

# Ripples in the baryon to dark matter ratio in $\Lambda$ CDM: implications for galaxy formation

Owen Jessop<sup>1,2\*</sup>, Adrian Jenkins<sup>1</sup>, Andrew Pontzen<sup>1</sup>, Joop Schaye<sup>3</sup>, Matthieu Schaller<sup>3,4</sup>, and John C. Helly<sup>1</sup>

<sup>1</sup>*Institute for Computational Cosmology, Department of Physics, Durham University, South Road, Durham, DH1 3LE, United Kingdom*

<sup>2</sup>*Centre for Extragalactic Astronomy, Department of Physics, Durham University, South Road, Durham, DH1 3LE, United Kingdom*

<sup>3</sup>*Leiden Observatory, Leiden University, PO Box 9513, 2300 RA Leiden, the Netherlands*

<sup>4</sup>*Lorentz Institute for Theoretical Physics, Leiden University, PO box 9506, 2300 RA Leiden, the Netherlands*

Accepted XXX. Received YYY; in original form ZZZ

## ABSTRACT

We use the FLAMINGO galaxy formation model to quantify the impact of baryon–CDM isocurvature perturbations on galaxy formation in  $\Lambda$ CDM. In linear theory, these perturbations represent local, compensated variations in the ratio between the baryon and CDM densities; they freeze in amplitude at late times, with an RMS amplitude of 1.5% on the Lagrangian scale of a  $10^{11} M_{\odot}$  halo (0.85 Mpc). Although such perturbations arise naturally within  $\Lambda$ CDM, most cosmological simulations and semi-analytic models to date omit them. These perturbations are strongly anti-correlated with the matter overdensity field such that halos form with baryon fractions below the cosmic mean, with earlier-collapsing halos exhibiting stronger baryonic suppression. To isolate the galaxy response, we analyse three hydrodynamical simulations with identical initial matter overdensity fields that: i) include isocurvature modes, ii) omit them, or iii) invert their amplitude. At  $z = 8$ , isocurvature perturbations reduce the mean baryon fraction and star formation rates of resolved halos by 5% and 12%, respectively, relative to the null-isocurvature case. These effects show no systematic dependence on halo mass and diminish steadily with time, reaching 0.1% and 1% by  $z = 0$ . We develop a model based on spherical collapse that accurately reproduces the mean baryon fraction suppression. As high-redshift observations become increasingly routine, incorporating isocurvature perturbations into simulations and semi-analytic models will be important for robust predictions of early galaxy and black hole formation in the *JWST* era.

**Key words:** software: simulations – galaxies: formation – galaxies: evolution – galaxies: high-redshift

## 1 INTRODUCTION

Prior to recombination, baryons and photons formed a tightly coupled relativistic fluid that supported acoustic oscillations on sub-horizon scales (Peebles & Yu 1970). These oscillations suppressed the growth of baryonic perturbations on scales below the sound horizon, in contrast to cold dark matter (CDM), which grew unimpeded via gravity after matter–radiation equality (e.g. Eisenstein & Hu 1998; Coles & Lucchin 2002). Shortly after recombination, the baryon and photon fluids decoupled, imprinting the acoustic oscillations in the matter distribution as the BAO signal observed in the late-time galaxy distribution (e.g. Eisenstein et al. 2005; Cole et al. 2005), and in the anisotropies of the CMB (e.g. Spergel et al. 2003; Aghanim et al. 2020). This decoupling left residual differences between the baryon and CDM density and velocity fields (e.g. Bond & Efstathiou 1984; Bardeen et al. 1986). The relative velocities, known as baryon–CDM streaming velocities, are coherent up to the BAO scale and remain supersonic with respect to the baryon sound speed after decoupling (e.g. Tseliakhovich & Hirata 2010). The accompanying relative density perturbations, known as baryon–CDM isocurvature perturbations, correspond to local, compensated variations in the ratio between

the baryon and CDM densities. Here, a local baryon deficit is exactly offset by a CDM excess, and vice versa, such that the matter overdensity, and therefore the gravitational potential and spacetime curvature, remains unchanged while power is redistributed between the two components. These perturbations sourced by baryon–photon decoupling are fundamentally distinct from the inflationary compensated isocurvature perturbations discussed in other studies (e.g. Heinrich & Schmittfull 2019; Barreira et al. 2020b), which arise in multi-field inflationary models and are not a generic prediction of  $\Lambda$ CDM.

After decoupling, baryons began to “catch up” by falling into the gravitational potential wells established by CDM. Initially, the baryon overdensity field exhibited negligible small-scale structure relative to CDM due to its prior coupling to photons. As gravitational infall proceeded, the clustering of the two components gradually converged: the baryon power spectrum was suppressed by  $\approx 50\%$  by  $z = 100$ ,  $\approx 20\%$  by  $z = 30$ , and  $\approx 10\%$  by  $z = 10$ . By the present day, these differences have largely been erased, with the baryon and CDM power spectra differing by  $\lesssim 1\%$  on scales above the Jeans length (e.g. Angulo et al. 2013). In contrast, the absolute amplitude of the baryon–CDM isocurvature overdensity field remains effectively frozen in amplitude at late times (e.g. Naoz & Barkana 2007; Khoraminezhad et al. 2021; Hahn et al. 2021), preserving a mem-

\* E-mail: owen.jessop2@durham.ac.uk

ory of the pre-decoupling baryon–photon oscillations. At late times, matter perturbations continue to grow whereas isocurvature modes remain approximately fixed in amplitude, rendering their influence most significant during the earliest phases of non-linear structure formation. This naturally raises the question of how strongly such perturbations can modulate early galaxy formation.

High-redshift galaxy formation has been revolutionised by the launch of the James Webb Space Telescope (*JWST*; Gardner et al. 2023), which has opened an observational window onto a previously inaccessible regime and discovered numerous bright galaxies at  $z \gtrsim 10$ . Over the coming decade, ground-based facilities such as the Extremely Large Telescope (*ELT*; Padovani & Cirasuolo 2023), and the Giant Magellan Telescope (*GMT*; Kautz et al. 2024) will complement *JWST* with deep, high-resolution spectroscopy and spatially resolved observations of the high-redshift galaxy population. Together, these facilities will significantly deepen our understanding of galaxy formation in the first billion years after the Big Bang, thereby placing increasingly stringent demands on theoretical models to reproduce the emerging high-redshift landscape.

These observations are typically interpreted through comparisons with predictions from cosmological simulations of galaxy formation. However, historically many simulations treated baryons and CDM as tracers of a single effective mass-weighted baryon+CDM (matter) fluid in the initial conditions (ICs), the so-called one-fluid approximation. This was motivated by the difficulty of generating accurate two-fluid baryon–CDM ICs (e.g. Angulo et al. 2013; Valkenburg & Villaescusa-Navarro 2017; Hahn et al. 2021), and by sizeable uncertainties in subgrid prescriptions that typically dwarfed any modest inaccuracies in the initial baryon–CDM distribution. Moreover, flagship simulation suites, such as OWLS (Schaye et al. 2010), EAGLE (Schaye et al. 2015), BAHAMAS (McCarthy et al. 2017), IllustrisTNG (Pillepich et al. 2017), HORIZON-AGN (Kaviraj et al. 2017), SIMBA (Davé et al. 2019), and MillenniumTNG (Pakmor et al. 2023), were designed to target low-redshift galaxy populations, where observational constraints are strongest and the effects of isocurvature perturbations are expected to be smallest. However, the landscape has been shifting in recent years: feedback models are becoming increasingly sophisticated and attention has been turning toward galaxy formation during the epoch of reionisation and beyond, as exemplified by simulation suites such as SPHINX (Rosdahl et al. 2018), FLARES (Lovell et al. 2020), THESAN (Kannan et al. 2021), SERRA (Pallottini et al. 2022), and MEGATRON (Katz et al. 2025). In this regime, the accuracy of the ICs becomes important, since neglecting the complete two-fluid baryon–CDM dynamics may introduce systematic biases in predictions of high-redshift observables.

Recent work by Rampf et al. (2020) and Hahn et al. (2021) has enabled the generation of higher-order two-fluid ICs that accurately reproduce the differential growth between baryons and CDM. These advances are implemented in the publicly available *MonofonIC* code<sup>1</sup> (Michaux et al. 2020; Hahn et al. 2021), which can generate up to third-order ICs for both Lagrangian and Eulerian simulations. The FLAMINGO (Schaye et al. 2023; Kugel et al. 2023) and COLIBRE (Schaye et al. 2025; Chaikin et al. 2025) simulation suites provided the first implementation of these improved two-fluid ICs within hydrodynamical simulations, but the impact of the two-fluid treatment has not been assessed within these models. In this study, we present a dedicated suite of three simulations using the FLAMINGO galaxy formation model to quantify the impact of baryon–CDM isocurvature perturbations on galaxy formation.

Most simulation-based work to date has focused on the baryon–CDM streaming velocity and its consequences for early galaxy formation. These studies show that a non-zero relative velocity delays the collapse of the first halos, suppresses the abundance of low-mass halos, reduces baryon fractions at high redshift, and postpones the onset of Population III star formation (e.g. Naoz et al. 2012; Fialkov 2014; Popa et al. 2016; Blazek et al. 2016; Schauer et al. 2019; Muñoz 2019; Park et al. 2020; Schauer et al. 2023). In contrast, the role of isocurvature density perturbations has been explored less thoroughly in simulations. Existing work on these perturbations is dominated by analytic or perturbative treatments that predict, for example, shifts in the BAO peak, modifications to the galaxy power spectrum, and a suppression of halo gas content, among other effects (e.g. Naoz & Barkana 2005; Barkana & Loeb 2005; Naoz & Barkana 2007; Barkana & Loeb 2011; Schmidt 2016; Chen et al. 2019). However, work exploring their effects in cosmological simulations, which is important for quantifying their impact on galaxy formation, remains relatively sparse and underdeveloped.

One of the earliest simulation-based comparisons of one-fluid and two-fluid ICs was carried out by Naoz et al. (2011). Using very small (2 Mpc) hydrodynamical simulations performed with GADGET-2 (Springel 2005), they quantified how two-fluid ICs modify the filtering mass and the degree of gas suppression at  $z \gtrsim 11$  relative to the one-fluid case, finding a pronounced redshift dependence in both quantities. However, their ICs also incorporated spatial variations in the baryonic sound speed (e.g. Naoz & Barkana 2005). For the low-mass, high-redshift halos they targeted, this additional effect is quite significant, making it difficult to isolate the influence of isocurvature density perturbations, which is our primary interest.

Only in recent years have isocurvature perturbations been investigated in large-volume cosmological simulations. Barreira et al. (2020a) introduced a long-wavelength isocurvature mode using the separate-Universe formalism,<sup>2</sup> globally reducing the mean baryon mass fraction by 5% across the simulation volume. Evolving this setup with the ILLUSTRISTNG model (Pillepich et al. 2017) and comparing to a control run, they measured a negative halo-bias parameter for the isocurvature component whose magnitude increases with halo mass and redshift, a 5% offset in the stellar mass–halo mass relation at low redshift, and sub-percent shifts in the galaxy power spectrum. As we will discuss, however, the strong anti-correlation between the isocurvature and matter overdensity fields complicates the interpretation of these results. Khoraminezhad et al. (2021) moved closer to a first-principles treatment by performing two-fluid gravity-only simulations with separate baryon and CDM fluids in the ICs. Their halo-bias measurements were broadly consistent with Barreira et al. (2020a), and they found that halo gas fractions at  $z = 0$  differ by  $\lesssim 1\%$  between dual- and single-fluid ICs. Bird et al. (2020) also adopted two-fluid ICs and evolved them with the galaxy formation model implemented in the MP-GADGET code (Feng et al. 2018). Their analysis focused on the one-dimensional Lyman- $\alpha$  forest power spectrum, where they identified  $\approx 10\%$  deviations relative to single-fluid ICs, but they did not explicitly investigate the consequence of isocurvature perturbations for galaxy formation.

To our knowledge, no previous study has combined two-fluid ICs with an advanced galaxy formation model in a large-volume hydrodynamical simulation to quantify how density isocurvature perturba-

<sup>1</sup> <https://bitbucket.org/ohahn/monofonic>

<sup>2</sup> The separate-Universe ansatz states that local structure formation within a long-wavelength perturbation in some fiducial cosmology is equivalent to global structure formation in an appropriately modified cosmology.

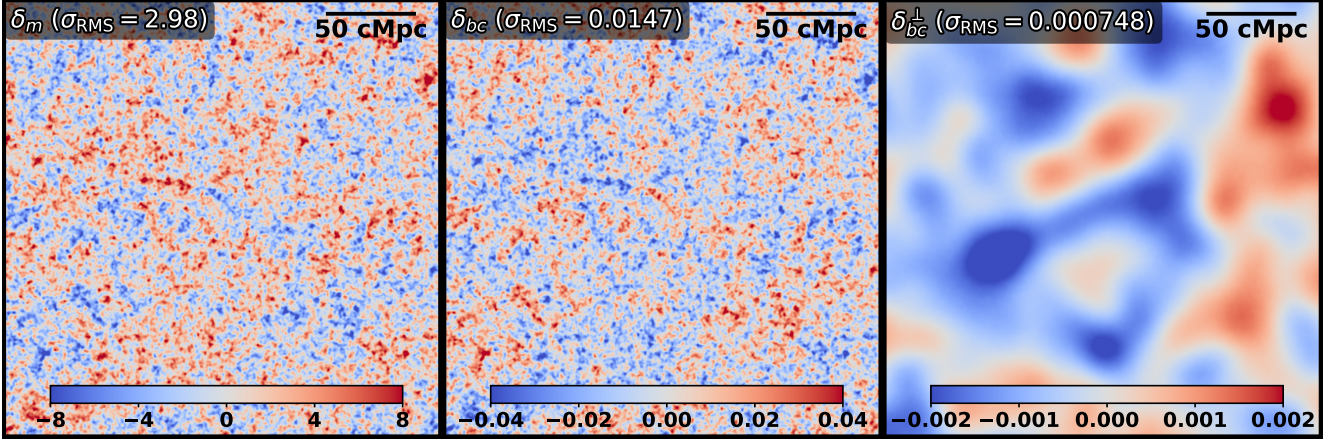


**Figure 1.**  $z = 0$  linear density fields computed with CLASS for the matter overdensity field,  $\delta_m$ , the isocurvature overdensity field,  $\delta_{bc}$ , and the orthogonal isocurvature overdensity field,  $\delta_{bc}^\perp$ ; see Eqs. (1) to (3). The fields have been smoothed with a spherical top-hat filter on the Lagrangian scale corresponding to a  $10^{11} M_\odot$  halo ( $R = 0.85$  Mpc). The cosmological parameters used correspond to the fiducial cosmology adopted throughout this paper (see Section 3.1). We sample the fields on a periodic 500 Mpc comoving cubic volume with  $900^3$  voxels; we display the central 250 Mpc region. Each panel shows an  $x$ - $y$  slice through the box centre with the root-mean-square (RMS) amplitude,  $\sigma_{\text{RMS}}$ , given in the upper left corner of each panel.

tions influence galaxy formation and propagate into late-time galaxy properties.

The structure of this paper is as follows. In Section 2, we introduce baryon–CDM isocurvature perturbations, explain their origin, describe their key properties, and examine their implications for galaxy formation. In Section 3.1 we provide a concise overview of the FLAMINGO galaxy formation model. In Section 3.2, we describe the generation of the FLAMINGO ICs and the modifications introduced for the simulations used in this work. Section 3.3 then outlines the method for the identification of (sub)halos and the software used to compute their properties. The main results are presented in Section 4 where we consider the effects of isocurvature perturbations on the galaxy population. Finally, in Section 5, we summarise our findings and discuss their broader implications for simulations of high-redshift galaxy formation.

## 2 BARYON–CDM ISOCURVATURE PERTURBATIONS IN $\Lambda$ CDM

After decoupling, baryons and CDM evolve jointly under gravity, effectively behaving as a single matter (baryon+CDM) fluid. However, the distinct pre-decoupling evolutionary histories leave residual perturbations in the relative density of the two fluids, manifesting as baryon–CDM isocurvature modes.

The matter overdensity field,  $\delta_m(\mathbf{x}, z)$ , is defined as

$$\delta_m(\mathbf{x}, z) \equiv \bar{f}_b \delta_b(\mathbf{x}, z) + \bar{f}_c \delta_c(\mathbf{x}, z), \quad (1)$$

where  $\mathbf{x}$  denotes the comoving position and  $z$  the redshift. The baryon and CDM overdensities,  $\delta_b$  and  $\delta_c$ , enter with weights given by their cosmic mean mass fractions,  $\bar{f}_b$  and  $\bar{f}_c$ , which satisfy  $\bar{f}_b + \bar{f}_c = 1$ . These fractions are defined by  $\bar{f}_b = \Omega_b/\Omega_m$  and  $\bar{f}_c = 1 - \bar{f}_b$ , where  $\Omega_b$  and  $\Omega_m$  are the present-day baryon and matter (baryons + CDM) density parameters, respectively. The matter overdensity field represents the mass-weighted combination of the two fluids and directly sources the gravitational potential to which both components respond, thereby determining the growth of cosmic structure.

The isocurvature overdensity field,  $\delta_{bc}(\mathbf{x}, z)$ , is defined as (e.g. Schmidt 2016)

$$\delta_{bc}(\mathbf{x}, z) \equiv \delta_b(\mathbf{x}, z) - \delta_c(\mathbf{x}, z), \quad (2)$$

which quantifies the relative density perturbation between baryons and CDM imprinted prior to decoupling. The field thus specifies whether a proto-halo region begins collapse with an enhanced or suppressed baryon fraction relative to the cosmic mean, and in this way  $\delta_{bc}$  modulates the baryonic reservoir available for galaxy formation once the region collapses non-linearly. In  $\Lambda$ CDM, linear-theory transfer functions imply a strong anti-correlation between  $\delta_m$  and  $\delta_{bc}$  on the mass scales relevant for early halo formation (e.g. Naoz & Barkana 2007; Schmidt 2016; Khoraminezhad et al. 2021). The origin and implications of this anti-correlation will be examined further in the following subsections.

### 2.1 Decomposition of the isocurvature overdensity field

The strength of the anti-correlation between  $\delta_{bc}$  and  $\delta_m$  can be understood by explicitly decomposing  $\delta_{bc}$  into the component proportional to  $\delta_m$  and a residual orthogonal component,  $\delta_{bc}^\perp$ ,

$$\delta_{bc}(\mathbf{x}, z) = \alpha(z) \delta_m(\mathbf{x}, z) + \delta_{bc}^\perp(\mathbf{x}, z), \quad (3)$$

with the projection coefficient  $\alpha(z)$  defined via the following inner product:

$$\alpha(z) \equiv \frac{\int \delta_{bc}(\mathbf{x}, z) \delta_m(\mathbf{x}, z) d^3\mathbf{x}}{\int \delta_m^2(\mathbf{x}, z) d^3\mathbf{x}}. \quad (4)$$

Fig. 1 shows the linear density fields at  $z = 0$  for  $\delta_m$ ,  $\delta_{bc}$ , and  $\delta_{bc}^\perp$ , calculated using the Einstein-Boltzmann code CLASS<sup>3</sup> (Lesgourgues & Tram 2011; Lesgourgues 2011). The fields have been smoothed with a spherical top-hat filter on the Lagrangian scale corresponding to a  $10^{11} M_\odot$  halo (0.85 Mpc). On this scale, the strong

<sup>3</sup> <http://class-code.net/>

anti-correlation between  $\delta_m$  and  $\delta_{bc}$  is immediately evident: the two fields exhibit almost identical structures but with opposite, rescaled amplitudes. By contrast, the orthogonal component  $\delta_{bc}^\perp$  is a very low-amplitude, visibly smoother field with a coherence length comparable to the BAO scale. In the realisation shown,  $\delta_{bc}^\perp$  contributes only 4.9% of  $\sigma_{\text{RMS}}(\delta_{bc})$  at  $z = 0$  on this scale. On proto-halo scales, the local amplitude of  $\delta_{bc}$  is therefore almost entirely determined by the local amplitude of  $\delta_m$ .

The anti-correlation between the two fields originates in the pre-decoupling dynamics of the baryon and CDM fluids. Prior to decoupling, baryonic perturbations were strongly suppressed, leading to  $\delta_m \approx \bar{f}_c \delta_c$  and  $\delta_{bc} \approx -\delta_c$ , implying near-perfect anti-correlation. After decoupling, baryonic pressure becomes almost negligible, and the two fluids evolve at essentially the same rate above the Jeans scale<sup>4</sup> under the influence of their shared gravitational potential:  $\delta_m$  follows the dominant growing mode, while  $\delta_{bc}$  comprises a linear combination of a constant mode and a decaying relative-velocity mode (e.g. [Hahn et al. 2021](#)). As the Universe expands, the relative-velocity mode is rapidly damped, eliminating any remaining differential growth between the fluids and leaving only the constant mode. The amplitude of  $\delta_{bc}$  therefore freezes out, asymptotically approaching a constant RMS amplitude of 1.5% when smoothed on the Lagrangian scale corresponding to a  $10^{11} M_\odot$  halo<sup>5</sup>. For completeness, [Section A](#) presents a derivation of this behaviour in an Einstein–de Sitter (EdS) Universe, showing that the late-time asymptotic behaviour of  $\delta_{bc}$  arises naturally from cosmic expansion and that its amplitude is fixed at decoupling, growing by a factor of approximately three between decoupling and the present day.

Deviations from exact pointwise anti-correlation in real space arise because baryon–photon coupling imprints pronounced BAO structure in  $\delta_b$  that is not expressed in  $\delta_c$ , providing the physical origin of the orthogonal component. Despite its small amplitude, this component remains dynamically important: its coherence on BAO scales modulates the baryon fraction over tens of megaparsecs, correlates the assembly histories of halos in the same large-scale environment, and introduces scatter in  $\delta_{bc}$  at fixed  $\delta_m$ .

The orthogonal component directly sources the large-scale baryon–CDM streaming velocity,  $\mathbf{v}_{bc} \equiv \mathbf{v}_b - \mathbf{v}_c$ , first identified as dynamically important by [Tseliakhovich & Hirata \(2010\)](#). This velocity field acts as a coherent headwind that advects baryons relative to CDM potential wells. Although its amplitude decays over time,  $\mathbf{v}_{bc}$  retains large-scale coherence, delaying halo collapse, suppressing gas accretion onto shallow potential wells, and postponing Population III star formation, effects that are most significant at high redshifts ( $z \gtrsim 10$ ) and in low-mass halos ( $M \lesssim 10^7 M_\odot$ ) (e.g. [Fialkov 2014](#); [Popa et al. 2016](#); [Schauer et al. 2019, 2023](#)).

## 2.2 Predicting the effects of isocurvature perturbations on halo formation

In  $\Lambda$ CDM,  $\delta_m$  determines the gravitational potential and hence the initial phase of halo collapse, while the baryonic assembly that follows depends sensitively on the baryon fraction at collapse, which follows the cosmic mean but is locally modulated by  $\delta_{bc}$ . Because  $\delta_m$  and  $\delta_{bc}$  are strongly anti-correlated on proto-halo scales (see

[Section 2.1](#)), the earliest-collapsing, high-amplitude peaks in  $\delta_m$  correspond to the most baryon-deficient proto-halo regions, while later-collapsing, lower-amplitude peaks form from progressively less baryon-deficient regions.  $\delta_{bc}$  thus induces a coherent modulation of the initial baryon content that depends on collapse redshift. The orthogonal component of  $\delta_{bc}$  introduces additional large-scale correlated scatter at fixed  $\delta_m$ , but this contribution is small, as shown in [Section 2.1](#), and is likely subdominant for galaxy formation. The strength of this modulation can be quantified by evaluating  $\delta_{bc}$  at the time of collapse, since this fixes the halo’s initial baryon fraction.

We begin by relating the change in baryon fraction to the amplitude of  $\delta_{bc}$ . In linear theory, the change in the baryon fraction induced by isocurvature perturbations is

$$\frac{f_b}{\bar{f}_b} = 1 + (1 - \bar{f}_b) \delta_{bc}. \quad (5)$$

At late times,  $\delta_{bc}$  is effectively frozen in amplitude (e.g. [Hahn et al. 2021](#)), so the corresponding perturbation to the baryon fraction is likewise frozen and simply carried forward to the epoch of halo collapse. We now require a way to connect this linear-theory prediction to the baryon fraction of a halo collapsing at a given epoch. To do so, we adopt the spherical-collapse model ([Gunn & Gott 1972](#); [Press & Schechter 1974](#)), in which a proto-halo region collapses when its linearly extrapolated matter overdensity reaches  $\delta_{\text{crit}} \approx 1.686$ . On proto-halo scales, we can relate  $\delta_{bc}$  and  $\delta_m$  using the decomposition established in [Section 2.1](#), which shows that  $\delta_{bc}$  is well approximated by the linear projection of  $\delta_m$ ,

$$\delta_{bc}(\mathbf{x}, z) \approx \alpha(z) \delta_m(\mathbf{x}, z). \quad (6)$$

While  $\delta_m$  grows with the linear growth factor  $D(z)$ ,  $\delta_{bc}$  remains approximately constant at late times. We normalised  $D(z)$  such that  $D(z = 0) = 1$  and therefore

$$\alpha(z) = \frac{\alpha_0}{D(z)}, \quad \alpha_0 \equiv \alpha(z = 0). \quad (7)$$

Evaluating [Eq. \(6\)](#) and [Eq. \(7\)](#) at the collapse redshift  $z_{\text{coll}}$ , and imposing the spherical-collapse condition  $\delta_m(z_{\text{coll}}) = \delta_{\text{crit}}$ , yields

$$\delta_{bc}(z_{\text{coll}}) = \frac{\delta_{\text{crit}} \alpha_0}{D(z_{\text{coll}})}. \quad (8)$$

Finally, combining [Eq. \(8\)](#) with [Eq. \(5\)](#), we obtain a prediction for the change in baryon fraction of a proto-halo region collapsing at  $z_{\text{coll}}$ ,

$$\frac{f_b}{\bar{f}_b}(z_{\text{coll}}) = 1 + \frac{(1 - \bar{f}_b) \delta_{\text{crit}} \alpha_0}{D(z_{\text{coll}})} \approx 1 - \frac{0.0069}{D(z_{\text{coll}})}. \quad (9)$$

with  $\alpha_0 = -0.0049$  and  $\bar{f}_b = 0.0160$  in the fiducial cosmology adopted in this paper (see [Section 3.1](#)).

This expression links the collapse redshift directly to the isocurvature imprint on proto-halo scales: earlier collapse (smaller  $D$ ) corresponds to more negative  $\delta_{bc}$  and therefore a larger initial baryon deficit. This result rests on linear theory and the idealised spherical-collapse model, and thus omits halo tri-axiality along with the full non-linear dynamics of gravitational collapse, hydrodynamics, and other baryonic processes. Even so, [Eq. \(9\)](#) provides a clear baseline for comparison with the baryon-fraction changes measured in our simulations, enabling us to identify how non-linear collapse and baryonic physics amplify, diminish, or redistribute the linear imprint of  $\delta_{bc}$ .

[Barkana & Loeb \(2011\)](#) proposed an alternative model for estimating the impact of isocurvature perturbations on halo formation. They used the quantity  $r_{\text{LSS}}$  (first introduced by [Naoz & Barkana 2007](#)), defined as the ratio of  $\delta_b$  to  $\delta_m$  evaluated in Fourier space. This quantity is computed using CAMB ([Lewis et al. 2000](#)) as a function of redshift

<sup>4</sup> On very small scales, finite temperature and pressure effects continue to suppress baryonic perturbations even after decoupling.

<sup>5</sup> As with  $\delta_m$ , in the absence of CDM free streaming, the RMS amplitude of  $\delta_{bc}$  diverges as smaller and smaller scales are included, so the field must be smoothed to obtain a physically meaningful value.

and evaluated at an intermediate-scale mode,  $k = 1 / (\text{h Mpc})$ , where it serves as a proxy for the isocurvature-induced suppression of halo gas content. When compared with the simulations of [Naoz et al. \(2011\)](#), this model systematically under-predicted the gas suppression and required an empirical rescaling. Our prediction, based on the spherical-collapse model, can be extrapolated to the much higher redshifts considered by [Naoz et al. \(2011\)](#) and, for example, yields a gas suppression of 11% at  $z = 20$ . Although this represents an improvement, it still underestimates the gas suppression measured in their simulations. However, a detailed direct comparison is not feasible because their ICs includes the additional effect of the spatially varying baryonic sound speed (e.g. [Naoz & Barkana 2005, 2007](#)) which becomes important for the high-redshift ( $z \geq 11$ ), low-mass ( $M \sim 10^5 M_\odot$ ) halos they studied.

### 3 THE SIMULATIONS

#### 3.1 The FLAMINGO galaxy formation model

The FLAMINGO simulation suite<sup>6</sup> (Full-hydro Large-scale structure simulations with All-sky Mapping for the Interpretation of Next Generation Observations) ([Schaye et al. 2023](#); [Kugel et al. 2023](#)) comprises large-volume cosmological simulations calibrated to match the  $z = 0$  observed stellar mass function ([Driver et al. 2022](#)) and the gas mass fractions of galaxy clusters ([Kugel et al. 2023](#)). The FLAMINGO suite was run using the open-source gravity, hydrodynamics, and galaxy formation code SWIFT (SPH With Interdependent Fine-grained Tasking)<sup>7</sup> ([Schaller et al. 2024](#)) with the SPHENIX Smoothed Particle Hydrodynamics (SPH) scheme ([Borrow et al. 2022](#)). Baryonic physics is modelled with subgrid prescriptions for radiative cooling and heating ([Ploekinger & Schaye 2020](#)), star formation ([Schaye & Dalla Vecchia 2008](#)), stellar mass loss ([Wiersma et al. 2009](#); [Schaye et al. 2015](#)), supernova feedback energy ([Dalla Vecchia & Schaye 2008](#); [Chaikin et al. 2022, 2023](#)), BH seeding and growth, and thermal feedback from active galactic nuclei (AGN) ([Springel et al. 2005](#); [Booth & Schaye 2009](#); [Bahé et al. 2022](#)). All subgrid parameters were calibrated using Gaussian process emulators ([Kugel et al. 2023](#)).

Star formation in FLAMINGO follows the pressure-based subgrid model of [Schaye & Dalla Vecchia \(2008\)](#). Dense gas is placed on an effective equation of state intended to represent an unresolved multiphase interstellar medium and is stochastically converted into stars at a rate calibrated to reproduce the Kennicutt–Schmidt relation ([Kennicutt 1998](#)). Gas particles that satisfy the required proper density, overdensity, and temperature criteria are eligible for one-to-one conversion into collisionless star particles, which inherit the full mass of their progenitor gas particles.

Black hole accretion is modelled using a modified Bondi–Hoyle accretion prescription, capped at the Eddington limit (e.g. [Springel et al. 2005](#)), with the accretion rate boosted at high gas densities to account for the unresolved Bondi radius and multi-phase interstellar medium (e.g. [Booth & Schaye 2009](#)). Black holes are seeded by converting the densest gas particle in a halo into a collisionless black hole particle once the host halo exceeds  $M_{\text{halo}} = 2.757 \times 10^{11} M_\odot$ , as identified by the FoF algorithm. As this criterion depends only on halo mass, it is insensitive to the presence of isocurvature perturbations. Newly seeded black holes are assigned an initial subgrid mass of  $10^5 M_\odot$ .

We adopt the intermediate-resolution "m9" subgrid calibration of the FLAMINGO galaxy formation model, employing identical galaxy formation and feedback physics to those of the 2.8 Gpc flagship FLAMINGO run. The cosmological parameters are taken from the '3x2pt + all external constraints' Dark Energy Survey Year 3 (DES-Y3) results ([Abbott et al. 2022](#)):  $\Omega_m = 0.306$ ,  $\Omega_b = 0.0486$ ,  $\sigma_8 = 0.807$ ,  $H_0 = 68.1 \text{ km s}^{-1} \text{ Mpc}^{-1}$ ,  $n_s = 0.967$ .

The FLAMINGO simulations were initialised at  $z_i = 31$  and run to a final redshift  $z_f = 0$ , with  $z_i$  chosen to be as late as possible to limit discreteness errors and reduce computational cost, while still preceding shell-crossing so that perturbation theory remains valid.

For the simulations presented here, we adopt the same mass resolution as the FLAMINGO flagship run but evolve a smaller  $(500 \text{ Mpc})^3$  volume, adjusting the particle counts accordingly. This configuration allows us to retain the m9 baryon particle mass resolution while keeping the computational cost tractable, and enables us to accurately resolve halos with  $M \geq 10^{11} M_\odot$ . Our analysis uses 78 simulation snapshots spanning  $z = 8$  to  $z = 0$ .

#### 3.2 The initial conditions

The generation of ICs for our simulations follows the same procedure as for the original FLAMINGO suite, whose ICs were generated with a modified version of `MonofonIC`<sup>8</sup> ([Elbers et al. 2022](#)) that self-consistently incorporates massive neutrinos alongside the two-fluid baryon–CDM formalism of [Hahn et al. \(2021\)](#). Details of the neutrino implementation within FLAMINGO are provided in [Schaye et al. \(2023\)](#). Following [Rampf et al. \(2020\)](#), `MonofonIC` extends single-fluid Lagrangian perturbation theory (LPT) to a two-fluid system under the assumption that baryon pressure and temperature are negligible (i.e. a Jeans length much smaller than the scales of interest; e.g. [Hahn et al. 2021](#)). On sufficiently small scales this approximation formally breaks down, as  $\Lambda$ CDM predicts a scale-dependent baryonic sound speed sourced by spatial temperature fluctuations ([Naoz & Barkana 2005, 2007](#)). However, these effects are expected to be negligible for the scales and redshifts analysed here. Simple estimates based on the Jeans mass indicate that baryonic pressure becomes dynamically relevant only for haloes with masses of order  $10^5$ – $10^6 M_\odot$ , and detailed calculations and simulations are consistent with this range (e.g. [Gnedin & Hui 1998](#); [Gnedin 2000](#); [Barkana & Loeb 2001](#); [Naoz et al. 2009](#)). At the higher halo masses considered in this work, any associated temperature fluctuations can therefore be safely neglected.

In the framework of [Hahn et al. \(2021\)](#), the baryon and CDM overdensity fields are described by three linear modes: the dominant adiabatic growing mode sourced by the total gravitational potential, and two baryon–CDM isocurvature modes, consisting of a constant mode and a decaying mode associated with the baryon–CDM streaming velocity. Since standard LPT only self-consistently treats the growing mode, `MonofonIC` first generates particle displacements from the dominant growing-mode solution and then encodes the constant mode via local perturbations to the particle masses. The magnitude of these mass perturbations is set by the local amplitude of  $\delta_{bc}$  evaluated at late times, typically  $z = 0$ . The decaying mode is incorporated as a first-order correction to particle masses and velocities, thereby introducing the appropriate redshift dependence into the effective mass perturbations that encode  $\delta_{bc}$ . This treatment is well justified at late times, for which the decaying mode has already been strongly suppressed and can be regarded as a small correction; in this

<sup>6</sup> <https://flamingo.strw.leidenuniv.nl/>

<sup>7</sup> <https://swiftsim.com>

<sup>8</sup> <https://github.com/wullm/monofonic>

regime, the approximation reproduces the linear-theory evolution of the baryon and CDM density fields to high accuracy.

In this study, we perform a suite of three simulation variants designed to isolate the impact of density isocurvature perturbations on galaxy formation. For simplicity we omit the decaying mode—convergence tests in smaller-volume simulations (not shown) confirm that the relative-velocity contribution remains subdominant, since our simulations are not sensitive to the redshift or mass resolution ( $M \lesssim 10^7 M_\odot$  at  $z \gtrsim 10$ ) where streaming velocities significantly affect halo formation (e.g. [Fialkov et al. 2012](#); [Popa et al. 2016](#); [Schauer et al. 2019, 2023](#)). All three simulations share an identical Gaussian white-noise field drawn from a subregion of Panphasia ([Jenkins 2013](#)), ensuring that their initial matter overdensity fields are identical. The chosen white noise field matches that of the L2p8\_m9 FLAMINGO variant and the three simulations differ only in their initial particle masses, which determine the specific isocurvature modes:

- **FID (FIDUCIAL: Negatively correlated isocurvature):** Base-line run using the original MonofonIC particle masses, retaining isocurvature modes (apart from the small omitted decaying mode). This provides the closest realisation of  $\Lambda$ CDM.

- **NULL (NULL: No isocurvature):** Erases isocurvature by re-setting baryon and CDM particle masses to their respective global mean values. Identical to the single-fluid approximation used in many previous studies, in which baryons and CDM are initialised using the matter overdensity field.

- **INV (INVERSE: Positively correlated isocurvature):** Inverts the isocurvature amplitude by reflecting particle masses about their mean, creating isocurvature modes positively correlated with the matter overdensity. This is not a physical solution in  $\Lambda$ CDM, but constitutes a useful test case.

For the adopted cosmology and particle load, the mean particle masses are

$$\bar{m}_c = (5.65 \times 10^9) M_\odot, \quad \bar{m}_b = (1.07 \times 10^9) M_\odot, \quad (10)$$

for CDM and baryons, respectively. In the isocurvature simulations, the particle masses exhibit RMS fractional deviations of 1.82% for baryons and 0.34% for CDM, corresponding to the same absolute RMS mass deviation of  $1.95 \times 10^7 M_\odot$  for both components. Because the particle-mass perturbations are compensated by construction, the matter overdensity field is unchanged by these modifications. All three simulations therefore begin from identical initial matter overdensity fields, ensuring that any subsequent differences in galaxy formation arise solely from the imposed baryon–CDM isocurvature modes.

### 3.3 Structure & substructure identification

The identification of (sub)halos within our simulations is performed via a two-step procedure. First, field halos are identified using a standard FoF algorithm (Friends-of-Friends; [Press & Davis 1982](#)), producing FoF catalogues for each snapshot. The FoF algorithm links all pairs of particles separated by less than  $b$  times the mean inter-particle separation, with  $b = 0.2$  ([Davis et al. 1985](#)) adopted in this work, corresponding to an overdensity of approximately  $100 \rho_{\text{mean}}$  ([More et al. 2011](#)), where  $\rho_{\text{mean}}$  denotes the mean density of the Universe. Only CDM particles are considered as linkable. Baryonic particles (gas, stars, BHs) cannot directly form links to one another; instead, they only form links with CDM particles.

Second, substructures within these FoF groups are identified with

the HBT–HERONS<sup>9</sup> algorithm (Hierarchical Bound Tracing – Hydro-Enabled Retrieval of Objects in Numerical Simulations; [Moreno et al. 2025](#)). HBT–HERONS is an updated version of the history-based subhalo finder HBT+ ([Han et al. 2012, 2017](#)), featuring improved identification and tracking of subhalos in both dark matter–only and hydrodynamical simulations.

The properties of the (sub)halos identified by HBT–HERONS are computed using SOAP<sup>10</sup> (Spherical Overdensity and Aperture Processor; [McGibbon et al. 2025](#)). SOAP is a Python package that reads the (sub)halo centres and particle membership lists provided by the halo finder as input and calculates a variety of subhalo properties within different spherical and projected apertures from the particle data.

In this work, we adopt the spherical overdensity definition of halos and compute halo properties including all particles within  $R_{200}$ , the radius enclosing a mean density of  $200\rho_{\text{crit}}$ , where  $\rho_{\text{crit}}$  is the critical density of the Universe. To ensure that the halos in our analysis are sufficiently well resolved, we apply a minimum mass threshold of  $10^{11} M_\odot$ .

## 4 RESULTS

In this section we quantify the impact of baryon–CDM isocurvature perturbations on galaxy formation by comparing global quantities across our three simulations, using the halo definition described in [Section 3.3](#). We focus on global measures because no statistically significant halo-mass dependence was found at fixed redshift. Uncertainties on global quantities are estimated via jackknife resampling, in which each simulation volume is divided into eight subregions and each global quantity is recomputed while successively omitting one subregion, with the resulting variance capturing finite-volume and sample-variance effects. Although we present results for the INV simulation, our primary focus is the comparison between FID and NULL, which directly tests the commonly adopted approximation of neglecting baryon–CDM density differences in the initial conditions; the INV run instead provides a deliberately non-physical inversion of the isocurvature amplitude and serves as an internal consistency check. We restrict the analysis to redshifts  $z \leq 8$ , beyond which halo abundances become too sparse for robust interpretation.

### 4.1 The time evolution of the baryon and gas content of halos

In [Section 2.2](#), we showed that linear theory combined with spherical collapse predicts an isocurvature-induced baryon deficit in halos relative to the null isocurvature case, arising solely from differences in their Lagrangian patches. We now test whether these initially small variations persist through non-linear structure formation by examining the time evolution of the comoving baryon mass density in resolved halos,  $\rho_b^{\text{halos}}(z)$ , shown in the top panel of [Fig. 2](#). This quantity rises steeply from high redshift towards the present day; the first halos collapse from rare, high-amplitude peaks in the matter overdensity field, whereas lower-amplitude peaks that are far more numerous collapse later and dominate the mass budget at low redshift (e.g. [Fakhouri et al. 2010](#); [Behroozi et al. 2013, 2019](#)). Accordingly, the baryon mass density in resolved halos grows by nearly three orders of magnitude between  $z = 8$  (0.65 Gyr after the Big Bang) and  $z = 0$  (13.76 Gyr after the Big Bang), before levelling off as

<sup>9</sup> <https://github.com/SWIFTSIM/HBT-HERONS>

<sup>10</sup> <https://github.com/SWIFTSIM/SOAP>

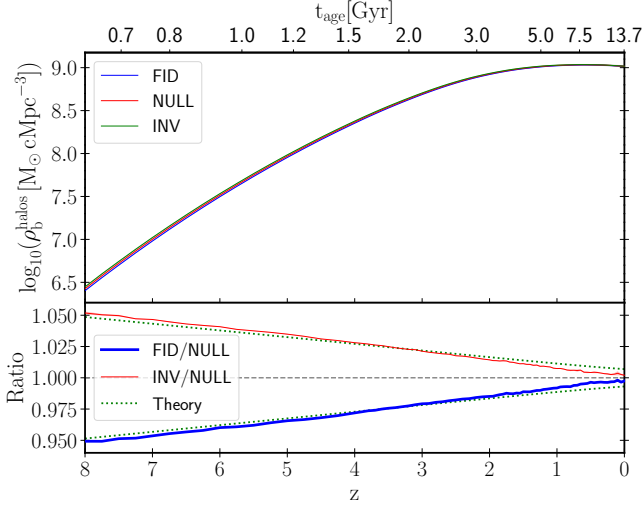


**Figure 2.** *Top panel:* The time evolution of the comoving baryon mass density in resolved halos,  $\rho_b^{\text{halos}}(z)$ , for our three different simulations. *Bottom panel:* The time evolution of the baryonic mass density in the FID and INV simulations relative to the NULL simulation, expressed as a ratio. The dotted green lines in the bottom panel represent the predictions of the theoretical model derived in Section 2.2, Eq. (9).

the rate of structure formation declines at late times. By  $z = 0$ , the incremental growth of  $\rho_b^{\text{halos}}(z)$  is small, indicating that most of the baryons destined to reside in collapsed systems have already been incorporated into virialised halos, even though a substantial fraction of cosmic baryons remain in the diffuse IGM (e.g. Péroux & Howk 2020; Tuominen et al. 2021; Yang et al. 2022).

The three simulations show nearly indistinguishable absolute values for  $\rho_b^{\text{halos}}(z)$ , particularly at low redshift, so to isolate the isocurvature response the bottom panel of Fig. 2 displays  $\rho_b^{\text{halos}}(z)$  in the FID and INV simulations expressed as ratios relative to the NULL simulation. The dotted green lines represent the predictions of the theoretical spherical collapse model derived in Section 2.2, Eq. (9). At  $z = 8$ , the isocurvature variants deviate from NULL by 5%, but this offset declines steadily to the sub-percent level by  $z = 0$ . The theoretical prediction, Eq. (9), provides an accurate estimate of the isocurvature-induced suppression measured in the simulations. It successfully reproduces the overall trend, including the sign of the modulation and the slope of the relation.

Having established the time evolution of the baryonic reservoir, we now consider the gas component in isolation. For clarity, we focus on the ratio of the isocurvature simulations relative to NULL, since our primary interest lies in the differential response between simulations. Panel (a) of Fig. 3 shows the time evolution of the comoving gas mass density in resolved halos,  $\rho_{\text{gas}}^{\text{halos}}(z)$ . At early times, when the Universe is still dominated by cold, unprocessed gas, this quantity closely traces the comoving baryon mass density in resolved halos,  $\rho_b^{\text{halos}}(z)$ , since the majority of baryons remain in the gaseous phase. As time advances, radiative cooling and gravitational collapse progressively funnel gas into dense regions where it is converted into stars, accreted onto BHs, or expelled due to feedback. This transition causes the gas mass to deviate from the baryonic mass, and the theoretical model to break down at late times.

The near-perfect antisymmetry of the FID and INV curves about the NULL baseline further confirms that this behaviour is a direct consequence of the sign of the  $\delta_{\text{bc}}-\delta_{\text{m}}$  (anti-)correlation. Positively

and negatively correlated isocurvature overdensity fields impose opposing initial gas deficits and surpluses, which in turn generate lower or higher gas fractions in halos that would otherwise form from identical matter overdensities.

A particularly notable late-time feature is the crossover in the gas ratios: for  $z \lesssim 0.7$ , the FID simulation exhibits a slightly higher collapsed gas mass than NULL, while INV falls modestly below it. The gradual convergence of the ratios toward unity can be partly explained by the fact that halos forming later are intrinsically less gas-deficient at formation; however, this effect alone cannot account for the reversal of the trend. The crossover instead arises from the coupled, time-dependent evolution of the gas reservoir, star formation, and feedback. In FID, the initial gas deficit suppresses early star formation and BH fuelling, thereby reducing early feedback and gas consumption. The opposite effect occurs in INV, where an initial gas surplus enhances early star formation and accretion activity, amplifying feedback and accelerating gas depletion.

#### 4.2 The time evolution of the stellar mass

The time evolution of the comoving star formation rate density,  $\dot{\rho}_{\text{star}}(z)$ , shown in panel (b) of Fig. 3, quantifies the instantaneous rate at which gas is converted into stars at each epoch per unit volume. Its evolution reflects the complex interplay between the supply of cold, star-forming gas and the competition among three key processes: gas accretion from the intergalactic medium, which feeds the gas reservoir; radiative cooling and gravitational collapse within halo potentials, which enable star formation; and feedback from massive stars, supernovae, and active galactic nuclei (AGN), which heat or expel gas and thereby regulate subsequent star formation (e.g. Madau & Dickinson 2014).

At  $z = 8$ , the FID simulation exhibits a 12% suppression of  $\dot{\rho}_{\text{star}}$  relative to NULL, whereas the INV simulation shows an approximately symmetric 12% enhancement. These early-time deviations reflect the initial modulation of halo gas content by  $\delta_{\text{bc}}$ , which either delays or accelerates the onset of cooling and star formation by altering the amount of gas available within each halo. The response of  $\dot{\rho}_{\text{star}}(z)$  is not directly proportional to that of  $\rho_{\text{gas}}^{\text{halos}}(z)$ . Instead, the star formation rate density exhibits offsets that are roughly twice as large, producing the late-time crossover seen in both quantities discussed in Section 4.1. This amplified behaviour arises because star formation responds non-linearly to the local gas density (e.g. Kennicutt 1998), and radiative cooling rates scale with the square of the gas density (e.g. Smith et al. 2017; Lee 2024).

The integrated consequence of these differences is captured by the time evolution of the comoving stellar mass density,  $\rho_{\text{star}}(z)$ , shown in panel (c) of Fig. 3. Here, the time evolution departs slightly from the near-perfect antisymmetry seen in the gas and star formation rates: the INV simulation displays a 12% enhancement in  $\rho_{\text{star}}(z)$ , while the FID run shows an 8% suppression at  $z = 8$ . Although the large jackknife uncertainties reflect the small stellar mass formed by this epoch, the asymmetry appears physical. It arises because the boosted gas supply in INV not only increases the instantaneous star formation rate but also accelerates its onset, giving an early advantage. Since  $\rho_{\text{star}}(z)$  is closely related to the time-integrated star formation rate, even symmetric differences in  $\dot{\rho}_{\text{star}}$  do not lead to symmetric totals. This early imbalance diminishes as stellar mass builds up, and by  $z = 5$  the isocurvature runs exhibit near-perfect symmetry about NULL, with only a 1% residual difference by  $z = 0$ . Thus, while isocurvature perturbations significantly modulate early star formation through their impact on gas content, their long-term

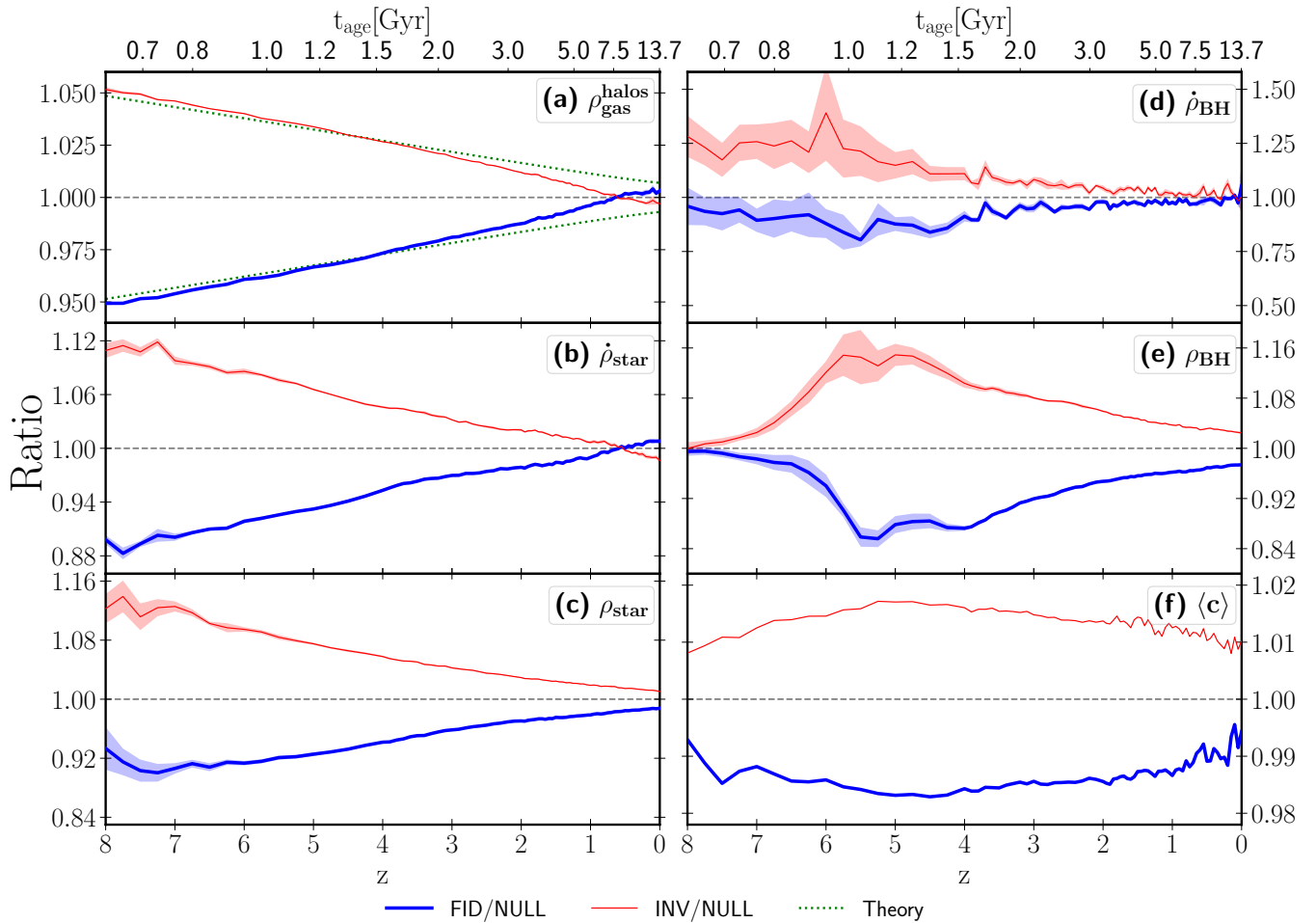


**Figure 3.** The time evolution of the ratio of various global quantities for the FID/NULL simulations (thick blue lines) and the INV/NULL simulations (thin red lines). The dotted green lines displayed in panel (a) represent the prediction of the theoretical model derived in Section 2.2, Eq. (9). Jackknife uncertainties have been computed for each quantity, propagated into the corresponding ratios, and are shown as shaded regions. Panel (a): the comoving gas mass density in resolved halos,  $\rho_{\text{gas}}^{\text{halos}}(z)$ ; Panel (b): the comoving star formation rate density,  $\rho_{\text{star}}(z)$ ; Panel (c): the comoving stellar mass density,  $\rho_{\text{star}}(z)$ ; Panel (d): the comoving BH accretion rate density,  $\dot{\rho}_{\text{BH}}(z)$ ; Panel (e): the comoving BH mass density,  $\rho_{\text{BH}}(z)$ ; Panel (f): The mean halo concentration,  $\langle c \rangle(z)$ .

influence on the integrated stellar mass budget is small within the FLAMINGO galaxy formation model.

### 4.3 The time evolution of the black hole mass

The growth of black holes (BHs) provides an especially sensitive probe of isocurvature perturbations, owing to the highly non-linear coupling between gas supply, accretion physics, and feedback. Panel (d) of Fig. 3 shows the time evolution of the comoving black hole accretion rate density,  $\dot{\rho}_{\text{BH}}(z)$ , a global, population-averaged quantity that measures the instantaneous rate at which gas is accreted onto the entire BH population per unit comoving volume at each epoch. The accretion histories are distinctly asymmetric between the INV/NULL and FID/NULL models. Jackknife uncertainties are substantially larger, particularly at high redshift, reflecting the fact that the global accretion rate is dominated by a few very highly accreting BHs, consistent with other works (e.g. Weinberger et al. 2025). At  $z = 8$ , INV is enhanced by 25% relative to NULL, whereas FID is mildly suppressed by 5%. This asymmetry arises from the coupling between the isocurvature-induced initial gas supply and

the complex, non-linear growth and feedback cycles governing BH evolution, whereby modest initial differences in gas supply are non-linearly amplified.

These differing accretion histories are manifested in the time evolution of the comoving BH mass density,  $\rho_{\text{BH}}(z)$ , shown in panel (e) of Fig. 3. At  $z = 8$ , the simulations agree to within  $\mathcal{O}(1\%)$ , as expected from the FLAMINGO seeding prescription; because compensated isocurvature modes leave halo collapse times effectively unchanged, the number of seeded BHs at fixed redshift is nearly identical across all runs. At these early epochs, insufficient time has elapsed for differences in accretion histories to generate appreciable differences in the BH populations. The jackknife uncertainties on  $\rho_{\text{BH}}(z)$  are substantially smaller than those on  $\dot{\rho}_{\text{BH}}(z)$ , consistent with the dominance of a few objects in setting the instantaneous global accretion rate.

Subsequently,  $\rho_{\text{BH}}$  diverges among the three simulations. In INV, the ratio to NULL rises rapidly and reaches a maximum offset of 15% by  $z = 6$ , driven by the larger accretion rate. The FID/NULL ratio shows a suppression of similar magnitude but evolves more gradually, peaking at 15% at a later epoch,  $z = 5.5$ . The near equality

of these peak amplitudes is initially counter-intuitive given the strong asymmetry in  $\dot{\rho}_{\text{BH}}$ . This arises because the BH population is growing extremely rapidly at early times: the comoving BH mass density increases by an order of magnitude over a short redshift interval, so even highly asymmetric instantaneous accretion rates integrate to a more symmetric cumulative effect. Thereafter the ratios evolve non-monotonically, briefly decreasing, then rising again before declining toward late times. By  $z = 0$  only a residual 3% offset in  $\rho_{\text{BH}}$  remains between the isocurvature and NULL runs. Among all diagnostics, the BH population thus retains the clearest late-time memory of isocurvature perturbations.

The greater symmetry in  $\rho_{\text{BH}}(z)$  compared with  $\dot{\rho}_{\text{BH}}(z)$  indicates that, despite the strongly asymmetric early accretion histories, the comoving BH mass density is regulated primarily by the sustained availability of gas. Although the global accretion rate at early times is dominated by a small number of BHs, the cumulative BH mass budget is distributed more evenly. Moreover, because the absolute accretion rates at high redshift are still small and increase steeply from snapshot to snapshot, the ratio of  $\rho_{\text{BH}}$  at any given epoch is set almost entirely by the accretion history in the short interval immediately preceding it.

#### 4.4 The time evolution of the mean halo concentration

The halo concentration,  $c$ , is a dimensionless measure of the central mass distribution of a halo and provides a useful diagnostic of whether isocurvature perturbations induce structural changes beyond their impact on the baryonic mass in halos. Panel (f) of Fig. 3 presents the ratio plots for the time evolution of the mean halo concentration,  $\langle c \rangle(z)$ , defined as the average value of  $c_{200}$  across all halos in the simulation volume. The halo concentration is computed following the method outlined in Wang et al. (2023), but employing a fifth-order polynomial fit to the  $R_1$ - $c$  relation over the range  $1 < c < 1000$ , where  $R_1$  denotes the first moment of the density distribution, under the assumption that halos follow a Navarro–Frenk–White (NFW) density profile (Navarro et al. 1997). In the FID simulation, isocurvature perturbations suppress the concentration by 1% at  $z = 8$ , rising to 1.5% suppression at  $z = 5$ , then returning to 1% by  $z = 0$ , with the INV simulations exhibiting a nearly mirrored trend. Although one might expect stronger suppression of the gas content at high redshift to reduce cooling and adiabatic contraction, thereby producing a redshift-dependent decline in concentration that tracks the gas deficit, the observed near time-independence of the suppression suggests that the underlying behaviour is more complex. Given the small amplitude and weak redshift evolution, we do not pursue this further here and conclude that halo concentrations are largely insensitive to the presence of isocurvature perturbations.

## 5 DISCUSSION & CONCLUSIONS

In this work we have presented a suite of three cosmological simulations performed with the FLAMINGO galaxy-formation model to quantify the impact of baryon–CDM isocurvature perturbations on key global galaxy properties. Introducing isocurvature perturbations into the ICs results in an average suppression of 5% in the comoving gas/baryon mass density of resolved halos at  $z = 8$ . The simulations show excellent agreement with the theoretical model developed in Section 2.2, which predicts the mean baryon suppression in halos induced by isocurvature perturbations. The reduced gas supply yields a 12% suppression in the comoving star formation rate density and a comparable reduction in the comoving stellar mass density. The

response of the comoving BH mass density lags the gas supply, with a maximum suppression of 15% at  $z = 5.5$ . The mean halo concentration exhibits a small response to isocurvature perturbations, with a suppression of just 1–2% that is weakly redshift dependent. These quantitative predictions should be interpreted in light of the scope of the FLAMINGO galaxy formation model, which was designed for studying structure formation in large cosmological volumes, at the expense of mass resolution and the detailed modelling of individual galaxies. The results reported here, other than the comoving baryon mass density in resolved halos, are therefore likely to be subgrid-model dependent.

Although the corrections introduced due to isocurvature perturbations are modest compared with present observational and subgrid-model uncertainties, their relative importance increases toward high redshift. The theoretical model presented in Section 2.2 predicts a 9% reduction in the gas content of halos collapsing at  $z = 15$ , which suggests a suppression of the comoving star formation rate density by over 20% at that epoch.

The high-redshift Universe at  $z \geq 10$ , until recently inaccessible, is now being probed by *JWST* (Gardner et al. 2023) surveys such as *JADES* (Bunker 2019) and *CEERS* (Finkelstein et al. 2023), which have reported unexpectedly luminous galaxies within the first few hundred million years after the Big Bang. These findings have prompted debate over whether they challenge  $\Lambda$ CDM or instead reflect limitations in current galaxy formation models (e.g. Menci et al. 2022; Wang & Liu 2023; McCaffrey et al. 2023; Gupta 2023; Lu et al. 2024; Stark et al. 2025). Our analysis shows that isocurvature perturbations induce an  $O(10\%)$  suppression in stellar mass and star formation rate densities at  $z = 8$ , with the effect increasing toward higher redshift. Although modest relative to present theoretical uncertainties, this systematic shift acts counter to the observed *JWST* excess, predicting fewer bright galaxies at early times and thereby marginally worsening the apparent tension. As observations continue to improve, accounting for these physically motivated corrections will be essential for robust comparisons between simulations, semi-analytic models, and data.

Another tension highlighted by *JWST* concerns the existence of numerous supermassive black holes (SMBHs) at high redshift. Deep observational campaigns have discovered quasars at  $z > 8$  hosting SMBHs with masses approaching  $10^9 M_{\odot}$  (e.g. Juodžbalis et al. 2023; Goulding et al. 2023; Maiolino et al. 2024; Pacucci & Loeb 2024; Juodžbalis et al. 2024), as well as a growing population of compact, extremely red sources, known as ‘little red dots’, whose morphologies, colours, and spectral signatures are consistent with actively accreting SMBHs (e.g. Labbé et al. 2023; Matthee et al. 2024; Kocovski et al. 2025). Taken together, these observations imply that black holes were assembling mass at extreme rates within the first few hundred million years after the Big Bang. Although the inferred masses and accretion rates remain subject to substantial selection effects and calibration uncertainties (e.g. Greene et al. 2024; Li et al. 2025), they lie systematically above local black hole–galaxy scaling relations (e.g. Pacucci et al. 2023; Harikane et al. 2023). Explaining such rapid early assembly lies beyond the reach of current large-volume cosmological simulations, which struggle to reconcile these high-redshift SMBHs with standard prescriptions for seeding, accretion, and feedback (e.g. Ni et al. 2022; Gordon et al. 2025).

The first BHs are believed to have formed in the dense centres of very high redshift halos ( $z \approx 20$ –30) either as Population III star remnants or via direct gas collapse (e.g. Devecchi et al. 2012; Yue et al. 2014; Latif & Ferrara 2016; Inayoshi et al. 2020; Regan & Volonteri 2024). Because both seeding channels depend sensitively on the gas reservoir at collapse, isocurvature perturbations will delay

seed formation and suppress early accretion rates. Simulations that neglect these perturbations consequently over-predict early gas densities, accretion rates, and BH masses; incorporating isocurvature perturbations instead yields a more gradual, physically motivated build-up of the high-redshift SMBH population.

In summary, isocurvature perturbations modulate galaxy formation in  $\Lambda$ CDM by reducing the gas content available at collapse, thereby influencing any subsequent process that depends on the initial gas reservoir. The effects of isocurvature perturbations are strongest at early times and almost negligible today. Incorporating these perturbations introduces a physically motivated correction that is absent from almost all current cosmological simulations and may exacerbate existing high-redshift observational tensions. Given that these perturbations can be implemented straightforwardly using IC codes such as *MonofonIC*, we recommend their routine inclusion in future simulation suites to improve the fidelity of high-redshift galaxy formation predictions within  $\Lambda$ CDM.

## ACKNOWLEDGEMENTS

The authors would like to thank the referee for their careful reading of the manuscript and for their constructive comments, which significantly improved the clarity and presentation of this work. We would also like to thank Shaun Brown, Martin Rey, and Oliver Hahn for their helpful comments on an earlier version of this manuscript. We are also grateful to the *FLAMINGO* collaboration for enabling this work and for providing useful assistance throughout its development. OJ is supported by UK Science & Technology Facilities Council (STFC) PhD Studentship ST/Y509346/1. ARJ and JCH are supported by STFC consolidated grant ST/X001075/1. AP is supported by the European Research Council (ERC) under the European Union's Horizon 2020 research and innovation program (Grant agreement No. 818085 GMGalaxies). For the purpose of open access, the author has applied a Creative Commons Attribution (CC BY) licence to any accepted manuscript version arising from this submission. The simulations and analyses of this project made use of the *DiRAC@Durham* facility managed by the Institute for Computational Cosmology on behalf of the STFC *DiRAC* HPC Facility ([www.dirac.ac.uk](http://www.dirac.ac.uk)). The equipment was funded by BEIS capital funding via STFC capital grants ST/K00042X/1, ST/P002293/1, ST/R002371/1 and ST/S002502/1, Durham University and STFC operations grant ST/R000832/1. *DiRAC* is part of the National e-Infrastructure.

## DATA AVAILABILITY

The data underlying the figures in this manuscript are available from the corresponding author upon reasonable request. While the complete raw simulation dataset spans several terabytes and cannot be readily distributed, the *SOAP* halo catalogues amount to only a few tens of gigabytes.

## REFERENCES

- Abbott T., Agüena M., Alarcon A., Allam 2022, *Physical Review D*, 105
- Aghanim N., et al., 2020, *A&A*, 641, A1
- Angulo R. E., Hahn O., Abel T., 2013, *MNRAS*, 434, 1756–1764
- Bahé Y. M., et al., 2022, *MNRAS*, 516, 167–184
- Bardeen J. M., Bond J. R., Kaiser N., Szalay A. S., 1986, *ApJ*, 304, 15
- Barkana R., Loeb A., 2001, *Physics Reports*, 349, 125–238
- Barkana R., Loeb A., 2005, *MNRAS Letters*, 363, L36–L40
- Barkana R., Loeb A., 2011, *MNRAS*, 415, 3113–3118
- Barreira A., Cabass G., Nelson D., Schmidt F., 2020a, *JCAP*, 2020, 005–005
- Barreira A., Cabass G., Lozanov K. D., Schmidt F., 2020b, *JCAP*, 2020, 049–049
- Behroozi P. S., Wechsler R. H., Conroy C., 2013, *ApJ*, 770, 57
- Behroozi P., Wechsler R. H., Hearin A. P., Conroy C., 2019, *MNRAS*, 488, 3143–3194
- Bird S., Feng Y., Pedersen C., Font-Ribera A., 2020, *JCAP*, 2020, 002–002
- Blazek J. A., McEwen J. E., Hirata C. M., 2016, *Physical Review Letters*, 116
- Bond J. R., Efstathiou G., 1984, *ApJ*, 285, L45
- Booth C. M., Schaye J., 2009, *MNRAS*, 398, 53–74
- Borrow J., Schaller M., Bower R. G., Schaye J., 2022, *MNRAS*, 511, 2367–2389
- Bunker A. J., 2019, *Proceedings of the International Astronomical Union*, 15, 342–346
- Chaikin E., Schaye J., Schaller M., Bahé Y. M., Nobels F. S. J., Ploeckinger S., 2022, *MNRAS*, 514, 249–264
- Chaikin E., Schaye J., Schaller M., Benítez-Llambay A., Nobels F. S. J., Ploeckinger S., 2023, *MNRAS*, 523, 3709–3731
- Chaikin E., et al., 2025, arXiv preprints, p. arXiv:2509.04067
- Chen S.-F., Castorina E., White M., 2019, *JCAP*, 2019, 006–006
- Cole S., et al., 2005, *MNRAS*, 362, 505–534
- Coles P., Lucchin F., 2002, *Cosmology: The Origin and Evolution of Cosmic Structure*. Wiley
- Dalla Vecchia C., Schaye J., 2008, *MNRAS*, 387, 1431–1444
- Davis M., Efstathiou G., Frenk C. S., White S. D. M., 1985, *ApJ*, 292, 371
- Davé R., Anglés-Alcázar D., Narayanan D., Li Q., Rafieferantsoa M. H., Appleby S., 2019, *MNRAS*, 486, 2827–2849
- Devecchi B., Volonteri M., Rossi E. M., Colpi M., Portegies Zwart S., 2012, *MNRAS*, 421, 1465–1475
- Driver S. P., et al., 2022, *MNRAS*, 513, 439–467
- Eisenstein D. J., Hu W., 1998, *ApJ*, 496, 605–614
- Eisenstein D. J., et al., 2005, *ApJ*, 633, 560–574
- Elbers W., Frenk C. S., Jenkins A., Li B., Pascoli S., 2022, *MNRAS*, 516, 3821–3836
- Fakhouri O., Ma C.-P., Boylan-Kolchin M., 2010, *MNRAS*, 406, 2267–2278
- Feng Y., Bird S., Anderson L., Font-Ribera A., Pedersen C., 2018, [doi:10.5281/ZENODO.1451799](https://doi.org/10.5281/ZENODO.1451799)
- Fialkov A., 2014, *International Journal of Modern Physics D*, 23, 1430017
- Fialkov A., Barkana R., Tselikhovich D., Hirata C. M., 2012, *MNRAS*, 424, 1335–1345
- Finkelstein S. L., et al., 2023, *ApJ Letters*, 946, L13
- Gardner J. P., Mather J. C., Abbott R., Abell J. S., Abernathy M., Abney e. a., 2023, *PASP*, 135, 068001
- Gnedin N. Y., 2000, *The Astrophysical Journal*, 542, 535–541
- Gnedin N. Y., Hui L., 1998, *Monthly Notices of the Royal Astronomical Society*, 296, 44–55
- Gordon S. T., Smith B. D., Khochfar S., Beckmann R. S., 2025, *MNRAS*, 537, 674–690
- Goulding A. D., et al., 2023, *ApJ Letters*, 955, L24
- Greene J. E., et al., 2024, *ApJ*, 964, 39
- Gunn J. E., Gott J. Richard I., 1972, *ApJ*, 176, 1
- Gupta R. P., 2023, *MNRAS*, 524, 3385–3395
- Hahn O., Rampf C., Uhlemann C., 2021, *MNRAS*, 503, 426–445
- Han J., Jing Y. P., Wang H., Wang W., 2012, *MNRAS*, 427, 2437–2449
- Han J., Cole S., Frenk C. S., Benítez-Llambay A., Helly J., 2017, *MNRAS*, 474, 604–617
- Harikane Y., et al., 2023, *ApJ Supplement Series*, 265, 5
- Heinrich C., Schmittfull M., 2019, *Physical Review D*, 100
- Inayoshi K., Visbal E., Haiman Z., 2020, *ARA&A*, 58, 27–97
- Jenkins A., 2013, *MNRAS*, 434, 2094–2120
- Juodžbalis I., et al., 2023, *MNRAS*, 525, 1353–1364
- Juodžbalis I., et al., 2024, *Nature*, 636, 594–597
- Kannan R., Garaldi E., Smith A., Pakmor R., Springel V., Vogelsberger M., Hernquist L., 2021, *MNRAS*, 511, 4005–4030
- Katz H., et al., 2025, arXiv preprints, p. arXiv:2510.05201

- Kautz M. Y., et al., 2024, *Journal of Astronomical Telescopes, Instruments, and Systems*, 10
- Kaviraj S., et al., 2017, *MNRAS*, p. stx126
- Kennicutt Jr. R. C., 1998, *ApJ*, 498, 541–552
- Khoramizhad H., Lazeyras T., Angulo R. E., Hahn O., Viel M., 2021, *JCAP*, 2021, 023
- Kocevski D. D., et al., 2025, *ApJ*, 986, 126
- Kugel R., et al., 2023, *MNRAS*, 526, 6103–6127
- Labbé I., et al., 2023, *Nature*, 616, 266–269
- Latif M. A., Ferrara A., 2016, *PASA*, 33
- Lee Y.-N., 2024, *A&A*, 684, A48
- Lesgourgues J., 2011, arXiv preprints
- Lesgourgues J., Tram T., 2011, *JCAP*, 2011, 032–032
- Lewis A., Challinor A., Lasenby A., 2000, *ApJ*, 538, 473
- Li J., et al., 2025, *ApJ*, 981, 19
- Lovell C. C., Vijayan A. P., Thomas P. A., Wilkins S. M., Barnes D. J., Irodoutou D., Roper W., 2020, *MNRAS*, 500, 2127–2145
- Lu S., Frenk C. S., Bose S., Lacey C. G., Cole S., Baugh C. M., Helly J. C., 2024, arXiv
- Madau P., Dickinson M., 2014, *ARA&A*, 52, 415–486
- Maiolino R., et al., 2024, *A&A*, 691, A145
- Matthee J., et al., 2024, *ApJ*, 963, 129
- McCaffrey J., Hardin S., Wise J. H., Regan J. A., 2023, *The Open Journal of Astrophysics*, 6
- McCarthy I. G., Schaye J., Bird S., Le Brun A. M. C., 2017, *MNRAS*, 465, 2936–2965
- McGibbon R., Helly J. C., Schaye J., Schaller M., Vandenbroucke B., 2025, *JOSS*, 10, 8252
- Menci N., Castellano M., Santini P., Merlin E., Fontana A., Shankar F., 2022, *ApJ Letters*, 938, L5
- Michaux M., Hahn O., Rampf C., Angulo R. E., 2020, *MNRAS*, 500, 663–683
- More S., Kravtsov A. V., Dalal N., Gottlöber S., 2011, *ApJ Supplement Series*, 195, 4
- Moreno V. J. F., Helly J., McGibbon R., Schaye J., Schaller M., Han J., Kugel R., Bahé Y. M., 2025, *MNRAS*
- Muñoz J. B., 2019, *Physical Review D*, 100
- Naoz S., Barkana R., 2005, *MNRAS*, 362, 1047–1053
- Naoz S., Barkana R., 2007, *MNRAS*, 377, 667–676
- Naoz S., Barkana R., Mesinger A., 2009, *Monthly Notices of the Royal Astronomical Society*, 399, 369–376
- Naoz S., Yoshida N., Barkana R., 2011, *MNRAS*, pp no–no
- Naoz S., Yoshida N., Gnedin N. Y., 2012, *ApJ*, 747, 128
- Navarro J. F., Frenk C. S., White S. D. M., 1997, *ApJ*, 490, 493–508
- Ni Y., et al., 2022, *MNRAS*, 513, 670–692
- Pacucci F., Loeb A., 2024, *ApJ*, 964, 154
- Pacucci F., Nguyen B., Carniani S., Maiolino R., Fan X., 2023, *ApJ Letters*, 957, L3
- Padovani P., Cirasuolo M., 2023, *Contemporary Physics*, 64, 47–64
- Pakmor R., et al., 2023, *MNRAS*, 524, 2539–2555
- Pallottini A., et al., 2022, *MNRAS*
- Park H., Ahn K., Yoshida N., Hirano S., 2020, *ApJ*, 900, 30
- Peebles P. J. E., Yu J. T., 1970, *ApJ*, 162, 815
- Pillepich A., et al., 2017, *MNRAS*, 473, 4077–4106
- Ploekinger S., Schaye J., 2020, *MNRAS*, 497, 4857–4883
- Popa C., Naoz S., Marinacci F., Vogelsberger M., 2016, *MNRAS*, 460, 1625–1639
- Press W. H., Davis M., 1982, *ApJ*, 259, 449
- Press W. H., Schechter P., 1974, *ApJ*, 187, 425
- Péroux C., Howk J. C., 2020, *ARA&A*, 58, 363–406
- Rampf C., Uhlemann C., Hahn O., 2020, *MNRAS*, 503, 406–425
- Regan J., Volonteri M., 2024, *The Open Journal of Astrophysics*, 7
- Rosdahl J., et al., 2018, *MNRAS*
- Schaller M., et al., 2024, *MNRAS*, 530, 2378–2419
- Schauer A. T. P., Glover S. C. O., Klessen R. S., Ceverino D., 2019, *MNRAS*, 484, 3510–3521
- Schauer A. T. P., Boylan-Kolchin M., Colston K., Sameie O., Bromm V., Bullock J. S., Wetzel A., 2023, *ApJ*, 950, 20
- Schaye J., Dalla Vecchia C., 2008, *MNRAS*, 383, 1210–1222
- Schaye J., et al., 2010, *MNRAS*, 402, 1536–1560
- Schaye J., et al., 2015, *MNRAS*, 446, 521–554
- Schaye J., et al., 2023, *MNRAS*, 526, 4978–5020
- Schaye J., et al., 2025, arXiv preprints, p. arXiv:2508.21126
- Schmidt F., 2016, *Physical Review D*, 94
- Smith T. L., Muñoz J. B., Smith R., Yee K., Grin D., 2017, *Physical Review D*, 96
- Spergel D. N., et al., 2003, *ApJ Supplement Series*, 148, 175–194
- Springel V., 2005, *MNRAS*, 364, 1105–1134
- Springel V., Di Matteo T., Hernquist L., 2005, *MNRAS*, 361, 776–794
- Stark D. P., Topping M. W., Endsley R., Tang M., 2025, arXiv
- Tselikhovich D., Hirata C., 2010, *Physical Review D*, 82
- Tuominen T., et al., 2021, *A&A*, 646, A156
- Valkenburg W., Villaescusa-Navarro F., 2017, *MNRAS*, 467, 4401–4409
- Wang D., Liu Y., 2023, arXiv
- Wang K., Mo H. J., Chen Y., Schaye J., 2023, *MNRAS*, 527, 10760–10776
- Weinberg S., 2008, *Cosmology*. Oxford University Press, Oxford
- Weinberger R., Bhowmick A., Blecha L., Bryan G., Buchner J., Hernquist L., Hlavacek-Larrondo J., Springel V., 2025, *A&A*, 700, A52
- Wiersma R. P. C., Schaye J., Theuns T., Dalla Vecchia C., Tornatore L., 2009, *MNRAS*, 399, 574–600
- Yang K. B., Wu Q., Wang F. Y., 2022, *ApJ Letters*, 940, L29
- Yue B., Ferrara A., Salvaterra R., Xu Y., Chen X., 2014, *MNRAS*, 440, 1263–1273

## APPENDIX A: THE TIME EVOLUTION OF BARYONS AND CDM IN AN EINSTEIN DE-SITTER UNIVERSE AFTER BARYON–PHOTON DECOUPLING

In Section 2.1, we showed that the isocurvature overdensity field,  $\delta_{bc}$ , is strongly anti-correlated with the matter overdensity field,  $\delta_m$ . This behaviour can be understood by specifying the conditions of the baryon and CDM fluids at baryon-photon decoupling and tracing their subsequent evolution. While the coupled baryon–CDM system generally requires a numerical solution, our aim is to construct a simple theoretical model to capture the origin of this anti-correlation on the scales relevant to structure formation. To this end, we consider the time evolution of the two fluids in an Einstein de–Sitter (EdS) Universe in which we ignore the effects of radiation, dark energy, and neutrinos.

We begin by introducing the baryon and CDM overdensity fields,  $\delta_b(\mathbf{x}, t)$  and  $\delta_c(\mathbf{x}, t)$ , defined at comoving position  $\mathbf{x}$  and time  $t$ . We neglect the self-gravity and pressure of baryons, assuming they respond to but do not contribute towards the gravitational potential. This approximation is valid shortly after baryon–photon decoupling on the scales of interest: photon drag had suppressed baryonic perturbations ( $\delta_b \ll \delta_c$ ), so that  $\delta_m$ , and hence the gravitational potential, is sourced predominantly by  $\delta_c$ .

In this EdS Universe,  $\delta_c(\mathbf{x}, t)$  is described by the following second-order differential equation (e.g. Weinberg 2008):

$$\ddot{\delta}_c(\mathbf{x}, t) + \frac{4}{3t} \dot{\delta}_c(\mathbf{x}, t) - \frac{2}{3t^2} \delta_c(\mathbf{x}, t) = 0, \quad (\text{A1})$$

The growing-mode solution for  $\delta_c(\mathbf{x}, t)$  and its time derivative  $\dot{\delta}_c(\mathbf{x}, t)$  are given by

$$\delta_c(\mathbf{x}, t) = A(\mathbf{x}) \left( \frac{t}{t_{\text{dec}}} \right)^{2/3}, \quad \dot{\delta}_c(\mathbf{x}, t) = \frac{2}{3t} \delta_c(\mathbf{x}, t), \quad (\text{A2})$$

where  $t_{\text{dec}}$  denotes the epoch of baryon–photon decoupling and  $A(\mathbf{x})$  is a dimensionless function defined such that  $A(\mathbf{x}) = \delta_c(\mathbf{x}, t = t_{\text{dec}})$ .  $\delta_b(\mathbf{x}, t)$  obeys a similar but inhomogeneous differential equation,

$$\ddot{\delta}_b(\mathbf{x}, t) + \frac{4}{3t} \dot{\delta}_b(\mathbf{x}, t) - \frac{2}{3t^2} \delta_c(\mathbf{x}, t) = 0, \quad (\text{A3})$$

and substituting Eq. (A2) gives

$$\ddot{\delta}_b(\mathbf{x}, t) + \frac{4}{3t} \dot{\delta}_b(\mathbf{x}, t) - \frac{2}{3} A(\mathbf{x}) t^{-4/3} t_{\text{dec}}^{-2/3} = 0. \quad (\text{A4})$$

Its general solution can be written as

$$\delta_b(\mathbf{x}, t) = \delta_c(\mathbf{x}, t) + C(\mathbf{x}) \left( \frac{t}{t_{\text{dec}}} \right)^{-1/3} + D(\mathbf{x}), \quad t \geq t_{\text{dec}}, \quad (\text{A5})$$

where  $C(\mathbf{x})$  and  $D(\mathbf{x})$  are dimensionless functions.

At decoupling  $\delta_b(\mathbf{x}, t)$  is effectively smooth and nearly static, allowing us to impose the following initial conditions

$$\delta_b(\mathbf{x}, t = t_{\text{dec}}) = 0, \quad \dot{\delta}_b(\mathbf{x}, t = t_{\text{dec}}) = 0, \quad (\text{A6})$$

which fixes the free functions

$$C(\mathbf{x}) = 2 \delta_c(\mathbf{x}, t = t_{\text{dec}}), \quad D(\mathbf{x}) = -3 \delta_c(\mathbf{x}, t = t_{\text{dec}}), \quad (\text{A7})$$

Combining these boundary conditions with the fact that  $\delta_c = \delta_m$  at decoupling, we find that the isocurvature overdensity field,

$$\delta_{bc}(\mathbf{x}, t) \equiv \delta_b(\mathbf{x}, t) - \delta_c(\mathbf{x}, t), \quad (\text{A8})$$

is given by

$$\delta_{bc}(\mathbf{x}, t) = -3 \delta_m(\mathbf{x}, t = t_{\text{dec}}) \left( 1 - \frac{2}{3} \left( \frac{t}{t_{\text{dec}}} \right)^{-1/3} \right), \quad t \geq t_{\text{dec}}. \quad (\text{A9})$$

This expression shows that the amplitude of  $\delta_{bc}$  is fully determined by the amplitude of  $\delta_m$  at decoupling. In the asymptotic time limit,

$$\delta_{bc}(\mathbf{x}, t \rightarrow \infty) = -3 \delta_m(\mathbf{x}, t = t_{\text{dec}}). \quad (\text{A10})$$

Within this model  $\delta_{bc}$  is anti-parallel to  $\delta_m$ , such that the two fields are perfectly anti-correlated. This derivation captures the essential origin of the anti-correlation and is consistent with the more general analyses of Rampf et al. (2020) and Hahn et al. (2021), who solve the coupled baryon–CDM system in a  $\Lambda$ CDM Universe under the assumption of negligible baryon temperature.

We test the accuracy of this asymptotic model by using it to predict the RMS amplitude of  $\delta_{bc}$  at  $z = 0$ , combining Eq. (A10) with the RMS amplitude of  $\delta_m$  at decoupling, computed using the Einstein–Boltzmann code CLASS. The prediction is then compared directly with the RMS amplitude of  $\delta_{bc}$  at  $z = 0$  obtained from CLASS. As in Fig. 1, the density fields are smoothed on the Lagrangian scale corresponding to a  $10^{11} M_\odot$  halo prior to evaluating the RMS. The asymptotic model yields  $\sigma_{\text{RMS}}(\delta_{bc}) = 0.0132$ , while CLASS gives  $\sigma_{\text{RMS}}(\delta_{bc}) = 0.0147$ , a relative difference of 10%. This close agreement demonstrates that the theoretical model captures the essential physics governing the time evolution of the baryon–CDM isocurvature mode and provides a quantitatively reliable estimate of its late time amplitude on the scales relevant for halo formation.

This paper has been typeset from a  $\text{\LaTeX}$  file prepared by the author.